Global drainage patterns and the origins of topographic relief on Earth, Mars, and Titan

Citation: Black, Benjamin A., et al. “Global Drainage Patterns and the Origins of Topographic Relief on Earth, Mars, and Titan.” Science, vol. 356, no. 6339, May 2017, pp. 727–31.

As Published: http://dx.doi.org/10.1126/SCIENCE.AAG0171

Publisher: American Association for the Advancement of Science (AAAS)

Persistent URL: http://hdl.handle.net/1721.1/118324

Version: Author's final manuscript: final author's manuscript post peer review, without publisher's formatting or copy editing

Global drainage patterns and the origins of topographic relief on Earth, Mars, and Titan

Authors: Benjamin A. Black[1,2*], J. Taylor Perron[3], Douglas Hemingway[4], Elizabeth Bailey[5], Francis Nimmo[6], Howard Zebker[7]

Affiliations:
[1] Department of Earth and Atmospheric Science, City College, City University of New York, New York City, NY USA

[2] Earth and Environmental Science, The Graduate Center, City University of New York, New York City, NY USA

[3] Department of Earth, Atmospheric, and Planetary Sciences, Massachusetts Institute of Technology, Cambridge, MA, USA

[4] Department of Earth and Planetary Science, University of California, Berkeley, Berkeley, CA, USA

[5] Division of Geological and Planetary Sciences, California Institute of Technology, Pasadena, CA, USA

[6] Department of Earth and Planetary Sciences, University of California, Santa Cruz, Santa Cruz, CA, USA

[7] Department of Geophysics, School of Earth Sciences, Stanford University, Stanford, CA, USA

*Correspondence to: bblack@ccny.cuny.edu

Abstract: Rivers have eroded the topography of Mars, Titan, and Earth, creating diverse landscapes. However, the dominant processes that generated topography on Titan (and to some extent on early Mars) are not well known. We analyze drainage patterns on all three bodies to show that large drainages—which record interactions between deformation and erosional modification—conform significantly better to long-wavelength topography on Titan and Mars than on Earth. We use a numerical landscape evolution model to demonstrate that short-wavelength deformation causes drainage directions to diverge from long-wavelength topography, as observed on Earth. We attribute the observed differences to ancient long-wavelength topography on Mars, recent or ongoing generation of long-wavelength relief on Titan, and creation of short-wavelength relief by plate tectonics on Earth.

One Sentence Summary: Global drainage patterns reveal differences in the origins and evolution of topography on Earth, Mars, and Titan.

Main Text:

Increasingly detailed observations of rocky and icy bodies in our solar system reveal dramatic diversity in surface topographic features. Plate tectonics has shaped topography extensively on Earth, but on less tectonically active worlds like Mars *(1-5)*, and icy worlds like Titan and Pluto *(6-8)*, the origins and history of the observed surface topography are varied and in some cases unknown. Fluid erosion offers a means to probe the long-term evolution of topography because drainage patterns interact with topography as it is uplifted and eroded *(e.g., 9)*. Fluid runoff has shaped the surfaces of at least three bodies in the solar system in the form of liquid water on Earth and Mars *(e.g., 10)* and liquid hydrocarbons on Titan *(e.g., 11, 12)*, thereby inscribing a record of how the development of landscapes has differed on these three worlds.

Earth's topography is dominated by the dichotomy between continents and ocean basins; most rivers drain from continental interiors to the ocean. However Earth's topography is also shaped by deformation concentrated near plate boundaries, such as the formation of collisional mountain ranges or volcanic arcs above subduction zones. These features can divert rivers as they traverse continents and can thereby displace drainage divides towards active margins, reshaping some of the planet's richest ecosystems in the process *(13)*. Many terrestrial river basins in tectonically active regions are continuously reorganized in response to changing tectonic boundary conditions *(9)*. As fluvial erosion (i.e., erosion by surface liquid flow) competes with tectonic deformation to shape Earth's landscapes, global drainage patterns should come to reflect a combination of long-wavelength, continent-scale topography and shorter-wavelength features such as mountain ranges.

Large-scale topography on Mars was established more than 3.5 billion years ago in the wake of the formation of Borealis Basin *(4, 14)* and the growth of the Tharsis volcanic rise *(1)*. Most fluvial activity likely occurred early in the planet's history *(5, 10, 15)*. On Titan, sparse impact craters and mountainous terrains attest to active modification of the surface *(16)*, though the age and origin of relief and the tempo of erosional modification remain to be determined *(11)*. We consider whether global drainage patterns differ on Earth and Mars as a result of their divergent geologic and surface histories, and we explore the implications of that comparison for Titan and other bodies where the erosional and tectonic history is largely unknown.

Our hypothesis is that on planets or moons where long-wavelength processes dominate production of relief, drainages should generally flow parallel to the slope of the long-wavelength topography, and the correlation should improve only marginally as the resolution of the topography is refined. We term the agreement between drainage patterns and topography at a given scale the drainage conformity with topography. In this context, we consider topography to be long-wavelength if it spans at least 1/40th of the planetary circumference; that is, spherical harmonics up to degree and order 20 (on Earth, ~1000 km). On bodies shaped by processes like plate tectonics that generate relief at shorter wavelengths, we expect reduced correlation at long wavelengths, with gradual improvement as shorter-wavelength features that deflect rivers are included in the comparison. We further hypothesize that the timing of deformation and erosion influences global drainage patterns. If the establishment of a planet's topography is followed by a long period of tectonic quiescence, rivers will have more time to adjust to—and alter—that topography, and drainage directions will conform better with the long-wavelength component of the altered topography. On planets where tectonic deformation is more recent or more intense than fluvial erosion, shorter-wavelength topography related to this deformation will have a stronger influence on drainage directions, and long-wavelength conformity will be reduced.

To test these hypotheses, we compared global drainage patterns and long-wavelength topography for Earth, Mars and Titan (Fig. 1). We focus on fluvially modified worlds, but we expect volcanic, cryovolcanic, and other fluid-flow features on bodies such as Venus and Pluto to leave similar signatures. We combined new and existing maps of drainages on Titan *(11, 12)*, Earth *(17)*, and Mars *(18)* with spherical harmonic models for topography *(19-22)*. We computed two proxy metrics for drainage conformity with topography (Fig. S1). The first metric, the downhill percentage (*%d*), represents the proportion of points along a river that are at higher elevations than the next downstream point for a given point spacing and spherical harmonic expansion of topography (Fig. 2A). As topographic resolution becomes finer—in this case, as topography is expanded to higher spherical harmonic degrees—*%d* should approach 100% for active drainage networks since liquids in open channels flow downhill. The second metric, the conformity factor (Λ), is defined as Λ= median(cos(δ)), where δ is the angle between the river drainage direction and the downslope direction of the topographic expansion (Fig. 2B). Values of Λ closer to 1 indicate better agreement between flow directions and long-wavelength topography, but we do not expect perfect conformity (Λ=1) at any resolution because we are comparing the steepest descent direction at a particular point to the flow direction across a finite interval.

Our results for topographic conformity as a function of maximum spherical harmonic degree are shown in Fig. 2. Conformity is consistently lower on Earth than on Mars or Titan, whereas Titan's conformity factor overlaps within uncertainty with that of Mars. The *%d* values are likewise much higher on Mars and Titan than on Earth. As expected, no body reaches near-perfect topographic conformity at the long wavelengths we consider here. These results lead us to the counterintuitive observation that many of Earth's rivers appear to flow sideways or uphill with respect to long-wavelength topography (as shown in Fig. 1B at locations where river traces deviate from gradient arrows), in contrast to most drainages on Titan and Mars.

On Mars, the strong correlation between valley network orientations and the present-day long-wavelength topography requires that most large-scale topography predates valley network formation in the Noachian era, and that this ancient topography was the dominant influence on valley network orientation (Fig. 1F) *(1, 2, 23)*. Martian topographic conformity remains imperfect even when shorter wavelengths are considered (Fig. S5). We attribute this persistent, moderate disagreement between drainage directions and topography to the combined effects of impact cratering, topographic resolution, and deformation after the era of valley network formation *(24, 25)*. Because *%d* quantifies the proportion of river segments that flow from higher to lower topography (Fig. 2A and S5), our results place bounds on the amount of vertical deformation after the era of valley network formation. For at least 85% of the fluvially dissected landscapes on Mars, Hesperian and Amazonian era vertical deformation has not exceeded the initial relief.

For Titan, a similar analysis suggests that mid-latitude and equatorial topography has been stable since the formation of the fluvial networks. If present-day topography was shaped by an episode of non-uniform crustal thickening at 0.3-1.2 Ga *(16, 26)*, fluvial networks at middle and low latitudes must have formed after that time. In contrast, many of Titan's north polar networks deviate from regional gradients (Fig. S3). This result is consistent with recent or ongoing predominantly short-wavelength deformation in the north polar region.

What processes have shaped the topographic conformity of Earth, Mars, and Titan? Multiple factors could plausibly contribute to weak long-wavelength topographic conformity, including little erosion relative to relief and resurfacing, low-amplitude long-wavelength topography, impact cratering, or vigorous short-wavelength deformation. However, Earth is deeply eroded, the topographic power spectra for the terrestrial planets are self-affine (i.e., the height of relief features scales with their wavelength), and topographic power spectra for the Earth and Mars are almost identical *(20, 27)*. Consequently, neither weak erosion nor contrasts in global static topography can fully explain the low topographic conformity on Earth relative to Mars.

On Earth, plate tectonics preserves cratons—broad, flat regions where small changes in topography can yield large shifts in conformity—while driving short-wavelength, spatiotemporally variable rock uplift at active margins. To explore the influence of terrestrial plate tectonics on drainage network evolution, we analyzed river network conformity for a series of numerical landscape evolution model simulations *(19, 28)*. We completed two sets of ten idealized simulations: the first set with spatially uniform uplift to represent a world in which long-wavelength deformation dominates the production of relief (Fig. 3A), and the second set with spatially variable uplift to capture the effects of short wavelength deformation on drainage orientations (Fig. 3B). The simulations with variable uplift are intended to investigate the particular influence of plate tectonics. According to both our metrics, drainage directions in the uniform uplift simulations conform much better with long-wavelength topography than in the variable uplift simulations (Figs. 3C and 3D). The absolute magnitudes of Λ and *%d* are higher in the model than in natural drainage networks, partly because the model lacks cratons and sedimentary basins, both of which suppress conformity in nature. Nonetheless, our idealized model offers qualitative insights into the effects of variable uplift on drainage patterns. Active, spatially variable uplift depresses topographic conformity, but this effect is temporary: once the variable uplift ceases, the topographic conformity steadily increases (Fig. S4A). Overall, the results support our hypothesis that short-wavelength active deformation (such as mountain-building on Earth) interferes with the background pattern of rivers draining the continents.

Geomorphic mapping shows that drainage basins on Mars are strongly influenced by pre-existing ancient Noachian topography, including the hemispheric dichotomy, early Noachian impact structures, and subtle ridges of unknown origin located throughout the southern highlands *(2, 23)*. Cratering during and after the ~4 Ga Late Heavy Bombardment further disrupted some drainage basins *(2, 23, 24)*. To quantify the extent of this disruption and the consequences for topographic conformity, we conducted additional landscape evolution simulations *(19)*. We find that unless impacts obliterate drainages entirely, they can modify but do not erase alignment with pre-existing long-wavelength topography (Fig. 4), consistent both with mapped relationships between drainage patterns and large-scale slopes *(1, 2, 23)* and with our measurements showing relatively high Martian topographic conformity. Crustal magnetization *(29)* and >3.6 Ga felsic rocks on Mars *(30)* have been interpreted as evidence for processes typically associated with plate tectonics on Earth. Our model results and the high conformity of Martian drainage networks suggest that at the time of Martian river incision, plate tectonics was absent and impact cratering was insufficiently intense to fully disrupt drainage alignment with ancient long-wavelength topographic gradients *(1, 2, 5, 23)*.

Of the three bodies we consider here, Titan's geologic history is the most enigmatic. In contrast to the ancient long-wavelength topography of Mars *(1, 4)*, Titan shows evidence for recent or ongoing geologic activity *(11, 16, 26).* Titan's long-wavelength conformity thus implies that long-wavelength mechanisms actively dominate the generation of relief in most regions of Titan (the north polar region is a possible exception). A mechanism such as global-scale changes in shell thickness due to tidal heating or basal melting and refreezing would create both long-wavelength relief and local fractures on Titan *(7, 31)*. Titan's high topographic conformity supports geophysical arguments for significant sediment transfer from topographic highs to lows *(31)*. Patterns in Titan's atmospheric circulation are expected to result in net poleward transport of hydrocarbons from mid-latitudes *(32)*. Of the drainages we mapped on Titan that are located poleward of 45 °N and 45 °S latitudes, and that traverse at least two degrees of latitude, five out of six drain towards the poles (Fig. 1; Database S1). This implies that other hydrocarbon fluxes or transport mechanisms must balance the net atmospheric and fluvial transport of hydrocarbons toward Titan's poles.

Topographic conformity does not reach the near-perfect *%d* predicted by the model on any of the three bodies we consider because of limited map resolution *(19)*. Modest short-wavelength deformation, impact cratering, or deformation after the development of drainages *(5, 25)* have probably also contributed to the imperfect conformity on Mars and Titan. The improvement of drainage alignment on Earth relative to Mars at very short wavelengths *(24)* supports this interpretation for Mars. In a set of landscape evolution simulations in which uplift ceases entirely after a period of variable uplift, we find that topographic gradients on the resulting low-relief surfaces (similar to Earth's cratons) can eventually grow weak and chaotic at shorter wavelengths, allowing drainage patterns to retain the imprint of past conditions (Fig. S4B). On Earth, topographic conformity dips at scales of 750-1500 km, which we attribute to steep gradients in elevation from ocean basins to convergent margins to low-relief continental interiors.

Earth and Mars share similarly bimodal topography *(33)* but divergent global geology, proving that the distribution of elevations alone cannot reveal geologic evolution. The interaction of rivers with long-wavelength topography provides an alternative record of the generation of planetary relief. The formation and amalgamation of continental crust are processes that create dominantly long wavelength topography, as is the process that built the Martian hemispheric dichotomy. Construction of mountain ranges on Earth has a dominantly intermediate wavelength, necessarily smaller than the scale of continents. Martian drainage patterns reflect ancient long-wavelength topography that predates both valley network formation and Noachian-Hesperian bombardment *(2)*, confirming that Noachian Mars lacked global plate tectonics and bounding post-Noachian changes in Martian relief. Our results favor dominantly long-wavelength relief-generating mechanisms on Titan such as shell thickness variations arising from tidal heating *(6, 7)* or thermal expansion and contraction *(6)*. Together, the three river-worn bodies in our solar system provide a Rosetta stone for deciphering the imprint of tectonics on landscapes.

References

1. R. J. Phillips *et al*., Ancient geodynamics and global-scale hydrology on Mars. *Science*. **291**, 2587-2591 (2001).

2. R. P. Irwin, A. D. Howard, Drainage basin evolution in Noachian Terra Cimmeria, Mars. *Journal of Geophysical Research: Planets*. **107**(2002).

3. J. T. Perron, J. X. Mitrovica, M. Manga, I. Matsuyama, M. A. Richards, Evidence for an ancient martian ocean in the topography of deformed shorelines. *Nature*. **447**, 840-843 (2007).

4. J. C. Andrews-Hanna, M. T. Zuber, W. B. Banerdt, The Borealis basin and the origin of the martian crustal dichotomy. *Nature*. **453**, 1212-1215 (2008).

5. S. Bouley *et al*., Late Tharsis formation and implications for early Mars. *Nature*.(2016).

6. G. C. Collins *et al*., Tectonics of the outer planet satellites. *Planetary Tectonics*. **11**, 264 (2009).

7. F. Nimmo, B. Bills, Shell thickness variations and the long-wavelength topography of Titan. *Icarus*. **208**, 896-904 (2010).

8. J. M. Moore *et al*., The geology of Pluto and Charon through the eyes of New Horizons. *Science*. **351**, 1284-1293 (2016).

9. S. D. Willett, S. W. McCoy, J. T. Perron, L. Goren, C. Chen, Dynamic Reorganization of River Basins. *Science*. **343**(2014).

10. A. D. Howard, J. M. Moore, R. P. Irwin, An intense terminal epoch of widespread fluvial activity on early Mars: 1. Valley network incision and associated deposits. *Journal of Geophysical Research: Planets (1991–2012)*. **110**(2005).

11. B. A. Black, J. T. Perron, D. M. Burr, S. A. Drummond, Estimating erosional exhumation on Titan from drainage network morphology. *Journal of Geophysical Research*. **117**, E08006 (2012).

12. D. M. Burr, S. A. Drummond, R. Cartwright, B. A. Black, J. T. Perron, Morphology Of Fluvial Networks On Titan: Evidence For Structural Control. *Icarus*. **226**, 742-759 (2013).

13. C. Hoorn *et al*., Amazonia through time: Andean uplift, climate change, landscape evolution, and biodiversity. *Science*. **330**, 927-931 (2010).

14. H. V. Frey, J. H. Roark, K. M. Shockey, E. L. Frey, S. E. Sakimoto, Ancient lowlands on Mars. *Geophys. Res. Lett*. **29**(2002).

15. C. I. Fassett, J. W. Head, The timing of martian valley network activity: Constraints from buffered crater counting. *Icarus*. **195**, 61-89 (2008).

16. C. D. Neish, R. D. Lorenz, Titan’s global crater population: A new assessment. *Planetary and Space Science*. **60**, 26-33 (2012).

17. H. Wu *et al.*, A new global river network database for macroscale hydrologic modeling. *Water Resources Research*. **48**, W09701 (2012).

18. B. M. Hynek, M. Beach, M. R. Hoke, Updated global map of Martian valley networks and implications for climate and hydrologic processes. *Journal of Geophysical Research: Planets (1991–2012)*. **115**(2010).

19. Materials and methods are available as supplementary materials on Science Online.

20. M. A. Wieczorek, Gravity and Topography of the Terrestrial Planets. *Treatise on Geophysics*. **10**, 153-193 (2015).

21. H. A. Zebker *et al.*, Size and Shape of Saturn's Moon Titan. *Science*. **324**, 921-923 (2009).

22. C. Hirt, M. Kuhn, W. Featherstone, F. Göttl, Topographic/isostatic evaluation of new-generation GOCE gravity field models. *Journal of Geophysical Research: Solid Earth (1978–2012)*. **117**(2012).

23. R. P. Irwin, R. A. Craddock, A. D. Howard, H. L. Flemming, Topographic influences on development of Martian valley networks. *Journal of Geophysical Research: Planets*. **116**(2011).

24. W. Luo, T. Stepinski, Orientation of valley networks on Mars: The role of impact cratering. *Geophys. Res. Lett*. **39**(2012).

25. A. Lefort, D. M. Burr, F. Nimmo, R. E. Jacobsen, Channel slope reversal near the Martian dichotomy boundary: Testing tectonic hypotheses. *Geomorphology*.(2014).

26. G. Tobie, J. I. Lunine, C. Sotin, Episodic outgassing as the origin of atmospheric methane on Titan. *Nature*. **440**, 61-64 (2006).

27. D. L. Turcotte, A fractal interpretation of topography and geoid spectra on the Earth, Moon, Venus, and Mars. *Journal of Geophysical Research: Solid Earth (1978–2012)*. **92**, E597-E601 (1987).

28. J. T. Perron, W. E. Dietrich, J. W. Kirchner, Controls on the spacing of first-order valleys. *Journal of Geophysical Research-Earth Surface*. **113**(2008).

29. F. Nimmo, D. Stevenson, Influence of early plate tectonics on the thermal evolution and magnetic field of Mars. *Journal of Geophysical Research: Planets (1991–2012)*. **105**, 11969-11979 (2000).

30. V. Sautter *et al.*, In situ evidence for continental crust on early Mars. *Nature Geoscience*. **8**, 605-609 (2015).

31. D. Hemingway, F. Nimmo, H. Zebker, L. Iess, A rigid and weathered ice shell on Titan. *Nature*. **500**, 550-552 (2013).

32. T. Schneider, S. D. B. Graves, E. L. Schaller, M. E. Brown, Polar methane accumulation and rainstorms on Titan from simulations of the methane cycle. *Nature*. **481**, 58-61 (2012).

33. R. D. Lorenz *et al.*, Hypsometry of Titan. *Icarus*. **211**, 699-706 (2011).

34. B. W. Stiles *et al.*, Determining Titan surface topography from Cassini SAR data. *Icarus*. **202**, 584-598 (2009).

35. H. Zebker *et al.*, Titan's Figure Fatter, Flatter Than Its Gravity Field. *AGU Fall Meeting Abstracts*.(2012).

36. L. Iess *et al.*, The tides of Titan. *Science*. **337**, 457-459 (2012).

37. D. E. Smith *et al.*, The global topography of Mars and implications for surface evolution. *Science*. **284**, 1495-1503 (1999).

38. D. Smith, G. Neumann, R. Arvidson, E. Guinness, S. Slavney, Mars Global Surveyor laser altimeter mission experiment gridded data record. *NASA Planetary Data System*.(2003).

39. J. T. Perron, J. W. Kirchner, W. E. Dietrich, Formation of evenly spaced ridges and valleys. *Nature*. **460**, 502-505 (2009).

40. A. D. Howard, G. Kerby, Channel changes in badlands. *Geological Society of America Bulletin*. **94**, 739-752 (1983).

41. K. L. Ferrier, K. L. Huppert, J. T. Perron, Climatic control of bedrock river incision. *Nature*. **496**, 206-209 (2013).

42. K. X. Whipple, G. E. Tucker, Dynamics of the stream-power river incision model: Implications for height limits of mountain ranges, landscape response timescales, and research needs. *Journal of Geophysical Research-Solid Earth*. **104**, 17661-17674 (1999).

43. S. D. Willett, Orogeny and orography: The effects of erosion on the structure of mountain belts. *Journal of Geophysical Research: Solid Earth*. **104**, 28957-28981 (1999).

44. C. Vörösmarty, B. Fekete, M. Meybeck, R. Lammers, Global system of rivers: Its role in organizing continental land mass and defining land-to-ocean linkages. *Global Biogeochem. Cycles*. **14**, 599-621 (2000).

45. C. J. Barnhart, A. D. Howard, J. M. Moore, Long-term precipitation and late-stage valley network formation: Landform simulations of Parana Basin, Mars. *Journal of Geophysical Research: Planets*. **114**(2009).

46. E. S. Kite, A. Lucas, C. I. Fassett, Pacing early Mars river activity: Embedded craters in the Aeolis Dorsa region imply river activity spanned≳(1–20) Myr. *Icarus*. **225**, 850-855 (2013).

47. B. A. Ivanov, Mars/Moon cratering rate ratio estimates. *Space Science Reviews*., 87-104 (2001).

48. S. T. Stewart, G. J. Valiant, Martian subsurface properties and crater formation processes inferred from fresh impact crater geometries. *Meteoritics & Planetary Science*. **41**, 1509-1537 (2006).

49. N. K. Forsberg-Taylor, A. D. Howard, R. A. Craddock, Crater degradation in the Martian highlands: Morphometric analysis of the Sinus Sabaeus region and simulation modeling suggest fluvial processes. *Journal of Geophysical Research: Planets*. **109**(2004).

50. N. Mangold *et al.*, The origin and timing of fluvial activity at Eberswalde crater, Mars. *Icarus*. **220**, 530-551 (2012).

51. B. M. Hynek, R. J. Phillips, New data reveal mature, integrated drainage systems on Mars indicative of past precipitation. *Geology*. **31**, 757-760 (2003).

52. D. G. Tarboton, A new method for the determination of flow directions and upslope areas in grid digital elevation models. *Water Resour. Res.* **33**, 309-319 (1997).

53. W. J. Conover, W. Conover, *Practical nonparametric statistics* (Wiley and Sons, New York, NY, 1980).

54. M. Longnecker, R. Ott, *An introduction to statistical methods and data analysis* (Nelson Education, Toronto, Canada, 2001).

55. W. H. Smith, D. T. Sandwell, Global sea floor topography from satellite altimetry and ship depth soundings. *Science*. **277**, 1956-1962 (1997).

Acknowledgments: We thank Erik Chan for spot-checking Martian drainages. Three reviewers provided constructive feedback. BAB acknowledges NASA grant NNX16AR87G. We thank the Cassini team. The landscape evolution code Tadpole is available on GitHub.

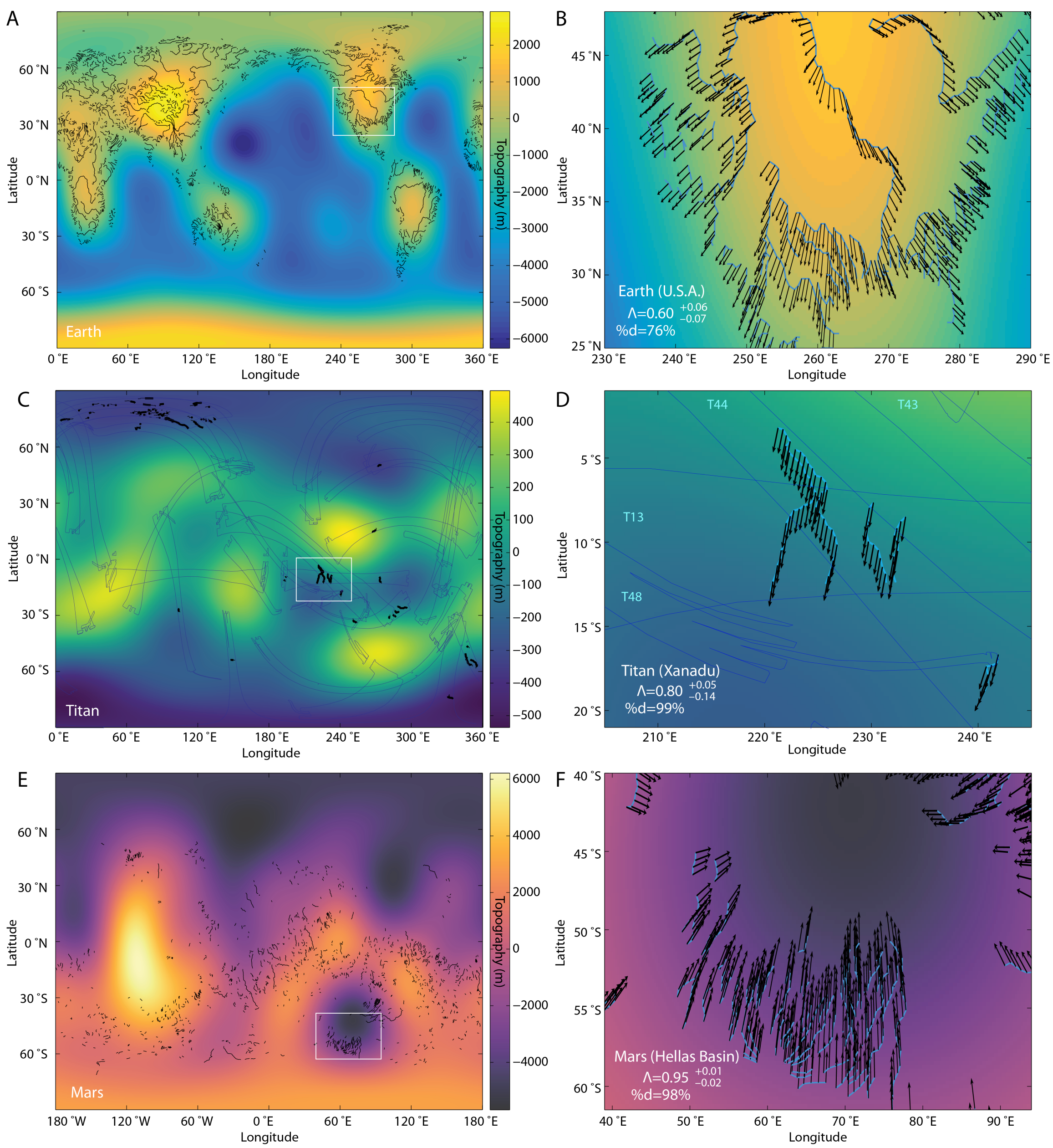

Fig. 1. Maps of topography referenced to the geoid and expanded to spherical harmonic degree and order 6, overlain with the fluvial features employed in this study. (A) Earth. **(B)** Enlargement of North America. **(C)** Titan. Blue outlines show Cassini Synthetic Aperture Radar observation swaths. **(D)** Enlargement of eastern Shangri-La and Xanadu regions of Titan. **(E)** Mars. **(F)** Enlargement of Hellas Basin on Mars. In **A, C, E,** white boxes outline regions enlarged in **B**, **D**, and **F**, where river courses are shown in blue; black arrows indicate topographic gradient at each point; and indicated conformity values span these enlarged regions, with uncertainties corresponding to the 95% confidence interval for the median.

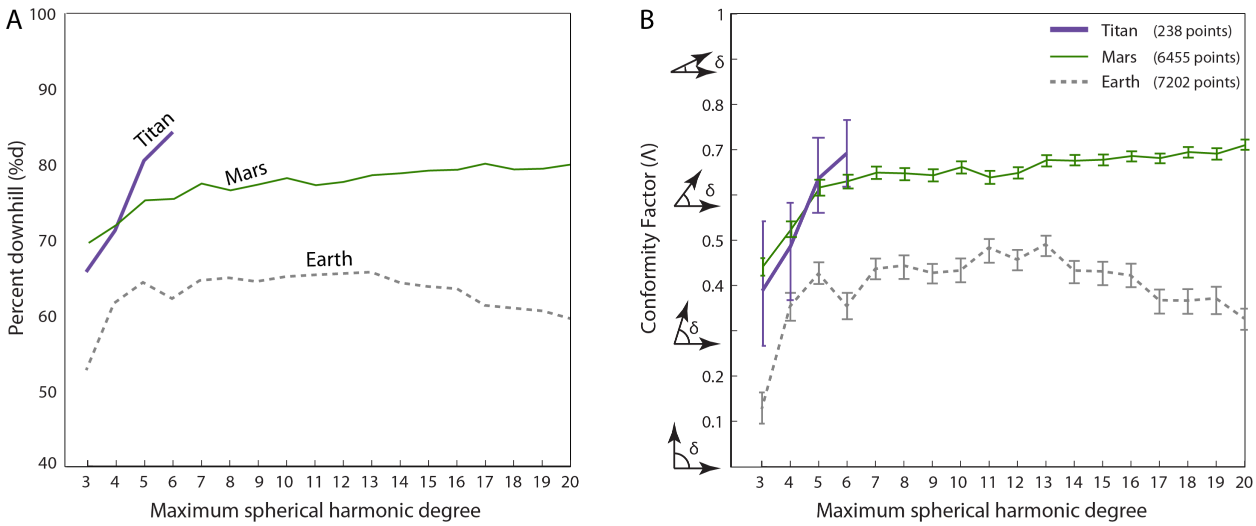

Fig. 2. Topographic conformity differs on Titan and Mars versus Earth. (A) The percent downhill (*%d*) metric as a function of the spatial resolution of the spherical harmonic expansion. **(B)** The conformity factor [Λ = median(cos(δ))]. Angles corresponding to Λ values illustrated on vertical axis. Uncertainties correspond to the 95% confidence interval for the median *(19)*.

338

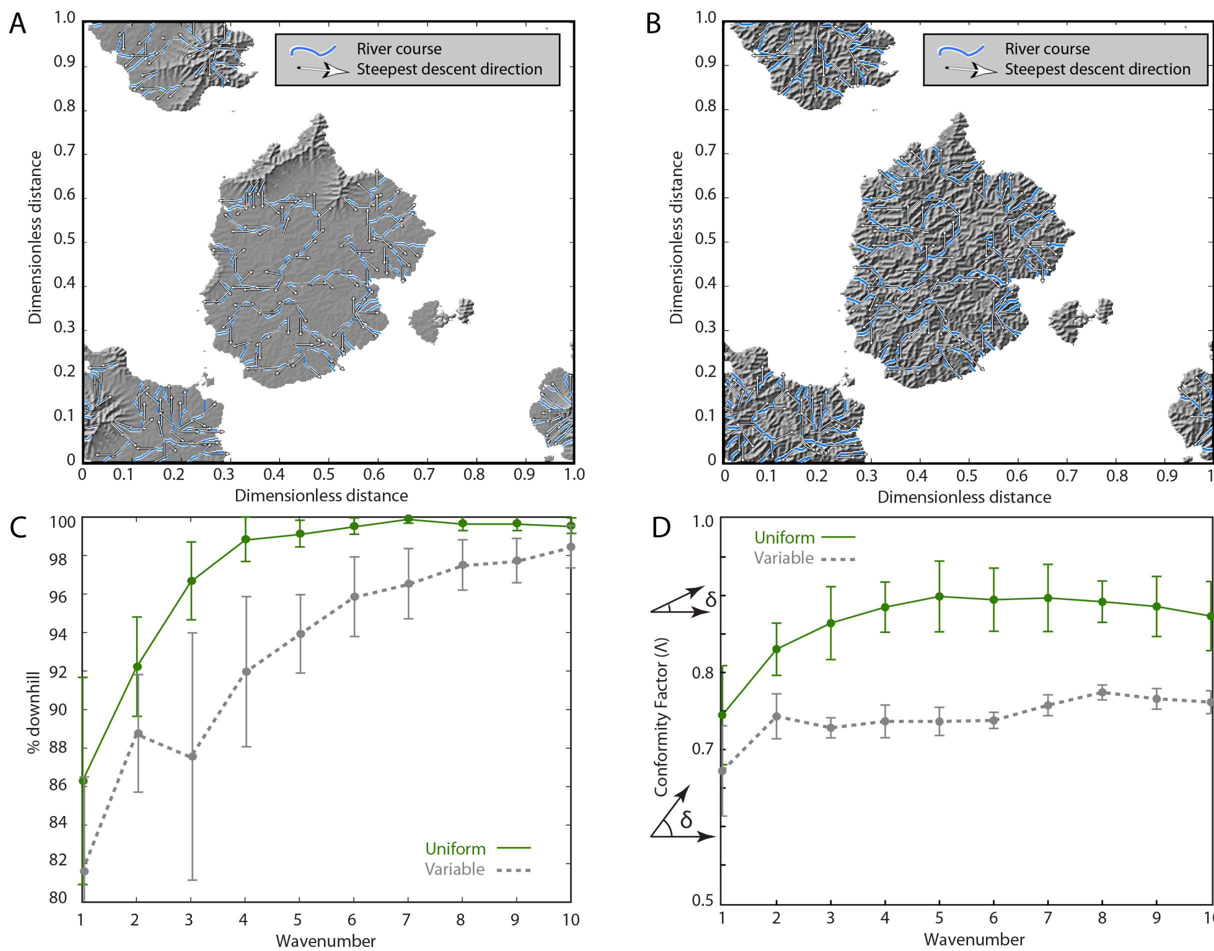

Fig. 3. Deformation history influences conformity. Variable uplift simulations **(A)** represent plate tectonic-style uplift; uniform uplift simulations **(B)** represent dominantly long-wavelength deformation. Shaded relief maps in **A** and **B** show simulations after 10 Myr. The model domain is doubly periodic, and the lowest 70% of initial elevations (white) were set as the base level relative to which uplift occurs. **(C)** Mean % downhill among 10 variable uplift simulations and 10 uniform uplift simulations. **(D)** Mean topographic conformity among the same simulations analyzed in C. In **C** and **D**, error bars represent two standard errors of the mean across the simulation ensembles.

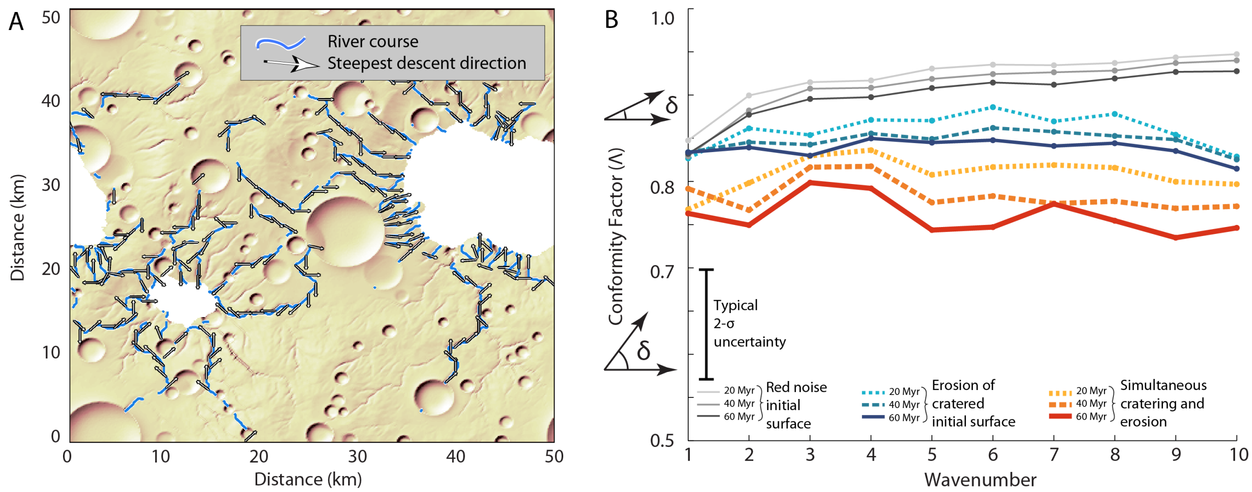

Fig. 4. Impact cratering can modulate topographic conformity. (A) Shaded relief map of a representative simulation after 60 Myr erosion in tandem with impact cratering. **(B)** Mean topographic conformity among 10 control simulations, 10 simulations with a cratered initial surface, and 10 simulations with ongoing cratering in tandem with fluvial erosion. Times refer to model time after initiation*(19)*. Legend shows a typical uncertainty of two standard errors of the mean within the simulation ensembles.

343

Supplementary Materials:

Materials and Methods

Figures S1-S8

Tables S1 and S2

Database S1

References (*34-55*)

Supplementary Materials for

Global drainage patterns and the origins of topographic relief on Earth, Mars, and Titan

Benjamin A. Black, J. Taylor Perron, Douglas Hemingway, Elizabeth Bailey, Francis Nimmo, Howard Zebker

Correspondence to: bblack@ccny.cuny.edu

This PDF file includes:

Materials and Methods
Figs. S1 to S8
Table S1 and S2
Caption for database S1

Other Supplementary Materials for this manuscript include the following:

Database S1 as .xlsx file

Materials and Methods

Our work relies on three principal datasets: maps of fluvial features on Titan, Earth, and Mars; spherical harmonic models for the topography of each of these bodies; and results from a numerical model of landscape evolution under a range of uplift conditions. We outline our methods for each dataset below.

Mapping fluvial features

Earth. To identify major fluvial features on Earth, we used 1/8th degree grids of global flow accumulation, basins, and flow length derived from orbital altimetry and corrected manually *(17)*. We identified each sink as a point of maximum flow accumulation within each basin, and the main trunk as the flow path linking each sink to the most distant point (along flow paths) within each basin. For rivers that spanned more than ~50 km, we identified sampling points at an interval of ~50 km, or every 5th grid point (the results are relatively insensitive to this selection; we chose this interval because it was sufficiently large to avoid sensitivity to the 1/8th degree resolution of the drainage dataset). We analyzed only rivers longer than this 50 km interval.

Mars. We relied on a global database of Martian river networks *(18)*. Sinks were identified as the topographically lowest extremities within each network; the validity of these sinks was spot-checked visually. The main trunk of each network was taken to be the path linking the most distal point within a network to the sink. We identified sampling points along this main trunk at an interval that matches the interval we used on Earth, but scaled by the ratio $Radius_{Mars}/Radius_{Earth}$ (this interval equates to ≈30 km on Mars). We analyzed only networks longer than this interval.

Titan. We manually selected 71 drainage networks from a global database compiled from the Cassini spacecraft's Synthetic Aperture Radar (SAR) swaths Ta to T71 *(12)*. These drainages were delineated on the basis of: i) linear geometry cross-cutting other SAR features; ii) light-dark pairings indicative of narrow topographic features; iii) branching geometries; iv) drainage into features interpreted as lakes *(11, 12)*. We selected drainages where we could confidently identify a sink location on the basis of junction angles, progressive downstream widening of valley features, orientation relative to features interpreted as lakes, and/or locally available stereo topography *(34)*. The source and sink coordinates we identified for all 71 networks we analyzed on Titan are given in Database S1. The main trunk of each network was taken to be the path linking the most distant point within a network to the sink. We identified sampling points along this main trunk at an interval that matches the interval we used on Earth, but scaled by the ratio $Radius_{Titan}/Radius_{Earth}$ (this interval equates to ≈21 km on Titan). We analyzed only networks longer than this interval. We defined a subset of North Polar networks as all eligible drainages with sinks located north of 60 °N latitude.

Spherical harmonic topography

We constructed spherical harmonic models of topography for Titan from RADAR-based topography *(21, 31, 35)* referenced to the geoid *(36)*; for Earth from the Earth2012 topography/bathymetry model (referenced to sea level) *(22)*; and for Mars from the Mars Orbiter

Laser Altimeter (MOLA)-derived, aeroid-referenced topography model *(37, 38)*. A robust spherical harmonic expansion for Titan's topography is available only up to degree (ℓ) 6 (ref. *(21)*). Titan has less long-wavelength relief than Earth or Mars (Fig. 1), indicating that the magnitude of topography alone cannot explain conformity. Our spherical harmonic models of terrestrial topography include bathymetry (Fig. S6). Oceanic basins form an integral part of Earth's plate tectonically derived topography (though the weight of the oceans deepens ocean basins, and fluvial erosion does not operate on the seafloor). Ancient oceans may also once have existed on Mars *(3)*.

Data availability

Coordinates for all drainage networks analyzed on Titan are available in spreadsheet form in Database S1. The data required to generate spherical harmonic topography for Earth, Titan, and Mars are available from the references provided in the text.

Landscape evolution model

Our landscape evolution model considers the effects of fluvial incision, uplift, and hill slope erosion (parameterized with a critical slope) on surface topography *(11, 28, 39)*. The model is available at https://github.com/MITGeomorph/Tadpole.

Variable vs. uniform uplift. The landscape evolution model solves the stream-power equation for the time evolution of fluvially eroded topography*(28, 39)*:

$$\frac{dz}{dt} = U - KA^m|\nabla z|^n \qquad \text{(S1)}$$

with elevation z, contributing area A, stream-power coefficient K, rate of uplift relative to a boundary U, m a constant taken to be 0.5*(40)*, and n a constant taken to be 1 *(41)*. Hill slope processes, which occur at finer scales than are of interest for comparison with our global topographic models, are approximated with a critical slope of 0.6, which prevents slopes from becoming unrealistically steep at drainage divides *(11)*.

The power-law relationship between incision rate and channel slope and contributing drainage area in Eq. (1) can be derived from the assumption that channel erosion rates scale with bed shear stress due to flow in a channel *(28, 40)*, and is motivated by the observed negative correlation between channel slope and contributing drainage area on Earth *(42)*. In our simulations, we assume a spatially constant stream-power coefficient, though in practice climatic and lithologic variations can lead to spatial variability in K *(41)*. Plate tectonics produces a patchwork of continental lithologies, and the orogenic feedback loop links mountain-building, exhumation, and climate *(43)*. The first effect might be expected to prolong the effects of plate tectonics in suppressing topographic conformity even after active deformation has ceased; the second effect might be expected to complicate the relationship between rock uplift, topography, and drainage patterns.

We derive a non-dimensional form of the governing equation following *(28)*:

$$\frac{dz'}{dt'} = \frac{KL^{2m}}{U} A'^{m}|\nabla' z'| + 1 \qquad \text{(S2)}$$

with $z = z'L$, $A = A'L^2$, $t = t'L/U$, $\nabla = \nabla'/L$. The lengthscale L is chosen to represent the distance from the drainage divide to the sink.

We initialize our simulations with randomly generated, autocorrelated initial topography; the lowest 70% of the initial surface is set to be a topographic sink as an analog for Earth's oceans (Fig. S7). We tabulate model parameter values in Table S1. In the simulations we analyzed, 13 ± 12% (1σ) of the land area is internally drained. For comparison, 14 ± 10% (1σ; the uncertainty reflects variability across continents) of Earth's unglaciated land area is internally drained *(44)*. To approximate the effects of plate tectonics, which localizes crustal thickening, the variable uplift cases have a pseudo-random pattern of autocorrelated, spatially non-uniform uplift superposed on the background uniform uplift field.

In place of spherical harmonic decompositions to characterize the model topography, we used 2-D Fourier transforms as described below.

Impact cratering. Impact cratering is one of the key mechanisms for relief generation on Mars. Crater counting of fluvial landscapes suggests that river activity reached a climax around the Noachian-Hesperian boundary, followed by a decline in activity that roughly coincided with waning cratering activity after the Late Heavy Bombardment *(10, 15)*. Landscape evolution modeling and crater counting further suggests that the terminal period of relatively intense fluvial activity lasted at least 10^3-10^4 years, and more likely spanned 10^5-10^7 years of episodic activity *(45, 46)*. Ancient large-scale topography on Mars, including the hemispheric dichotomy, predates fluvial incision *(1, 5)*. This topography may have been generated through basin-scale impacts *(4)* or through other unknown processes. Geomorphic mapping suggests that valley networks were strongly influenced by ancient topographic gradients, but that younger Noachian-Hesperian cratering did modify and disrupt some river paths *(2, 23)*.

To investigate and quantify the influence of impact cratering on topographic conformity, we ran three landscape evolution model ensembles, each with ten simulations (Fig. S8), in which we considered (i) an initial surface with randomly generated, autocorrelated initial topography (our control ensemble, which represents ancient topography without any younger, fresh craters), (ii) an initial surface with randomly generated, autocorrelated topography, with superposed impact craters (to represent erosion of ancient topography that has experienced more recent cratering), (iii) an initial surface with randomly generated, autocorrelated topography, with superposed impact craters, and with additional impact cratering occurring in tandem with fluvial erosion (to represent cratered, ancient topography that undergoes fluvial erosion in tandem with cratering, for example during the Late Heavy Bombardment).

To account for the greater occurrence of smaller craters, we assumed the size-frequency distribution for Martian impact craters as adapted from the lunar production function for craters 1-16 km in diameter *(47)*. The autocorrelated initial topography represents ancient topography, for example due to basin-forming impacts. However, we did not generate fresh craters larger than 16 km diameter, because our goal was to study the interaction of impacts with pre-existing topography and valley networks (and larger impacts obliterate both for our chosen grid size of 50 km by 50 km). We used scaling relationships for Mars highland craters *(48)* to calculate crater depths for the strength and gravity regimes, and we employed polynomial fits from *(48)* to calculate the shapes of axisymmetric cavities, rims, and uplift zones. Following *(49)*, we calculated the final topography outside the crater rim as a weighted average of the pre-impact topography and the impact-generated topography, where the weighting declines linearly from the rim to a distance of three radii from the crater center.

Our simulations to investigate impact cratering differ from those designed to investigate the effects of plate tectonic-style deformation in that for the purposes of accurate impact crater depth-diameter scaling, we have chosen to make these simulations dimensional. We used model grids that represented lateral dimensions of 50 km by 50 km, with 125 meter horizontal resolution. The complete list of parameters and parameter values used in the impact cratering simulations is given in Table S2. The true duration and rate of valley network incision on Mars are unknown *(10, 50)*, and the rate and duration trade off in the model to determine the total amount of incision. Trunk channels of Martian valley networks incised ~50 to 350 m into older terrains *(10)*, creating drainage densities of ~10^{-2} km^{-1} *(51)*. We selected values for K (see Table S2) and simulation duration (60 Myr) that generated cumulative erosion that qualitatively matched typical values of drainage density and trunk channel fluvial incision observed on Mars.

<u>Analysis</u>

The metrics we applied to compare drainage orientations with topography are illustrated graphically in Fig. S1. To avoid the need to weight fluvial features by size, and to integrate changes in flow direction and downslope direction along river courses, we performed both the %d and Λ analyses at intervals along the main trunks of major fluvial features (see Fig. S1).

Synthetic networks. The maximum size of observed drainage networks differs on Titan, Earth, and Mars, which might a priori influence the scale of topography reflected in drainage orientations. To avoid scale dependence in our comparison, we used a point spacing that is uniform relative to planetary radius on each body. To test whether our algorithm displays any bias related to drainage network scale, and to investigate the likelihood of false positive results, we repeated our analyses on synthetic datasets. These datasets comprised line segments of uniform length distributed and oriented randomly across the simulated landscape (Fig. S2). We generated 1,000-10,000 such synthetic segments for each test, and we analyzed the portion of those synthetic segments that crossed the landmasses in our simulations. In total, we conducted four tests on representative simulations from the ensemble analyzed in the manuscript: with line segments spanning either 1/2 or 1/20 the domain of our numerical simulations, and on landscapes in which our simulations included either uniform or variable uplift. In all cases, our analysis yielded statistically indistinguishable results with a topographic conformity of zero (Fig. S2, panels E-F). In other words, the random synthetic networks showed no preferred orientation relative to the topography, and our algorithm displayed no measureable bias due to systematic differences in drainage size. These tests support the robustness of our results for Titan, Earth, and Mars.

Downhill percentage (*%d*). At each upstream-downstream pair of sampling points along each drainage path, we determined whether the upstream point is at a higher elevation according to the topographic model at a given maximum degree. For each body (and each model run) %d is the percentage of all upstream-downstream pairs that pass (i.e. the upstream point has a higher elevation according to the model topography). At infinite resolution (or as wavenumber $k \rightarrow 200$

for the 400×400 model grids), *%d* should approach 100%, because liquid flows downhill with respect to the geoid.

Topographic conformity (Λ). At each sampling point along each drainage path, we determined δ, the angle between the steepest descent direction and the flow direction. For the planetary bodies, steepest descent was determined using MATLAB's `gradientm` function for the gradient on spheroidal bodies; for the model runs, steepest descent was calculated according to the D-infinity flow routing algorithm*(52)*. We calculated flow direction as the azimuth of the vector linking each sampling point to the next downstream point. We defined the topographic conformity at a given maximum spherical harmonic degree or wavenumber as the median value of cosine(δ) calculated at all sampling points: $\Lambda_\ell = \text{median}(\cos(\delta))$.

Uncertainties. The uncertainties indicated in Figure 1, 2, S2, and S3 represent the 95% confidence interval for the median. The 95% confidence interval for the median is bounded by the *j*th and *k*th observation in a ranked list of *n* observations, where *(53, 54)*:

$$j = n \times q - 1.96\sqrt{n \times q(1-q)}\ \text{, and }\ k = n \times q + 1.96\sqrt{n \times q(1-q)}\ .$$

Here $q = 0.5$, because by definition the median divides the dataset into two quantiles.

The uncertainties in Figure 3 represent two standard errors of the mean *%d* (Figure 3c) and Λ (Figure 3d) values across the ensemble of ten simulations with spatially variable uplift and ten simulations with spatially uniform uplift.

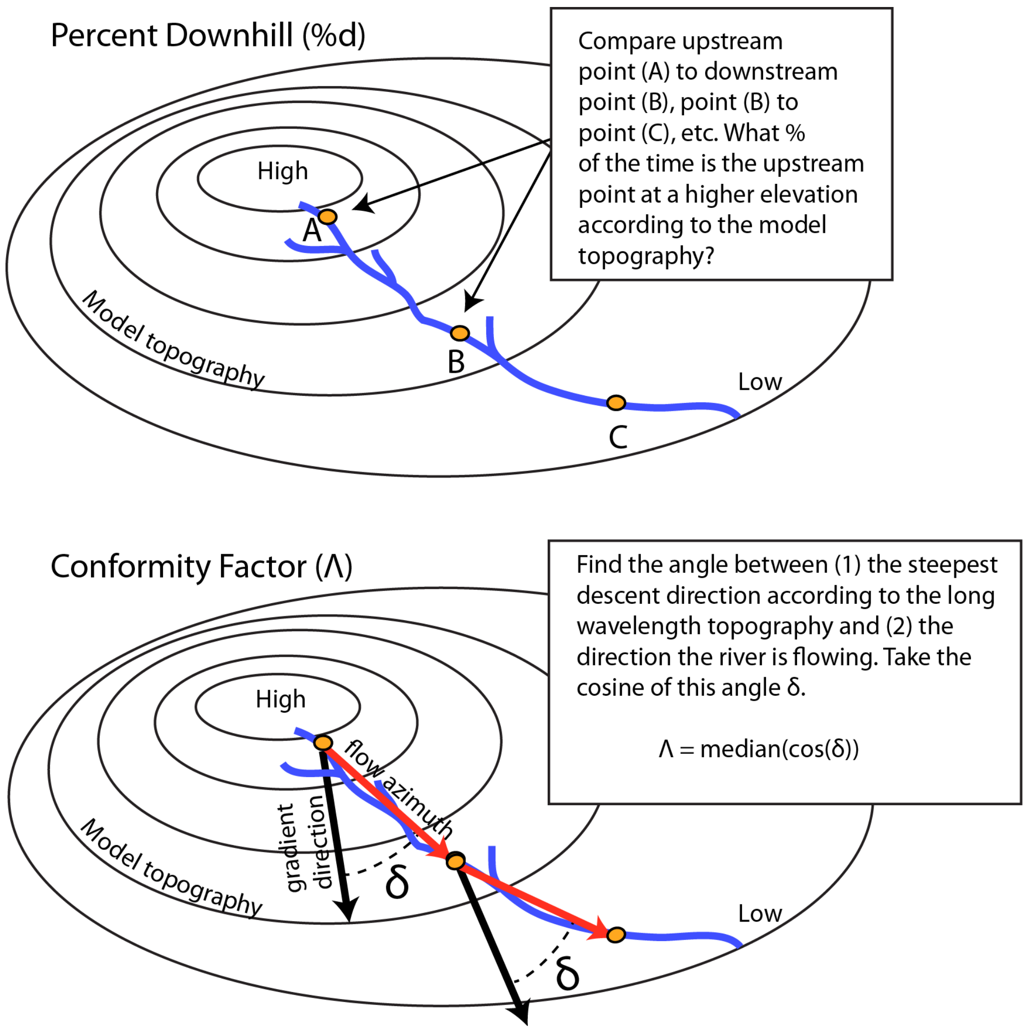

Fig. S1. Schematic illustration of two proxy metrics for the agreement between river orientations and topography at a given scale. The upper panel illustrates the definition of the percent downhill metric (*%d*) and the lower panel the definition of the conformity factor (Λ).

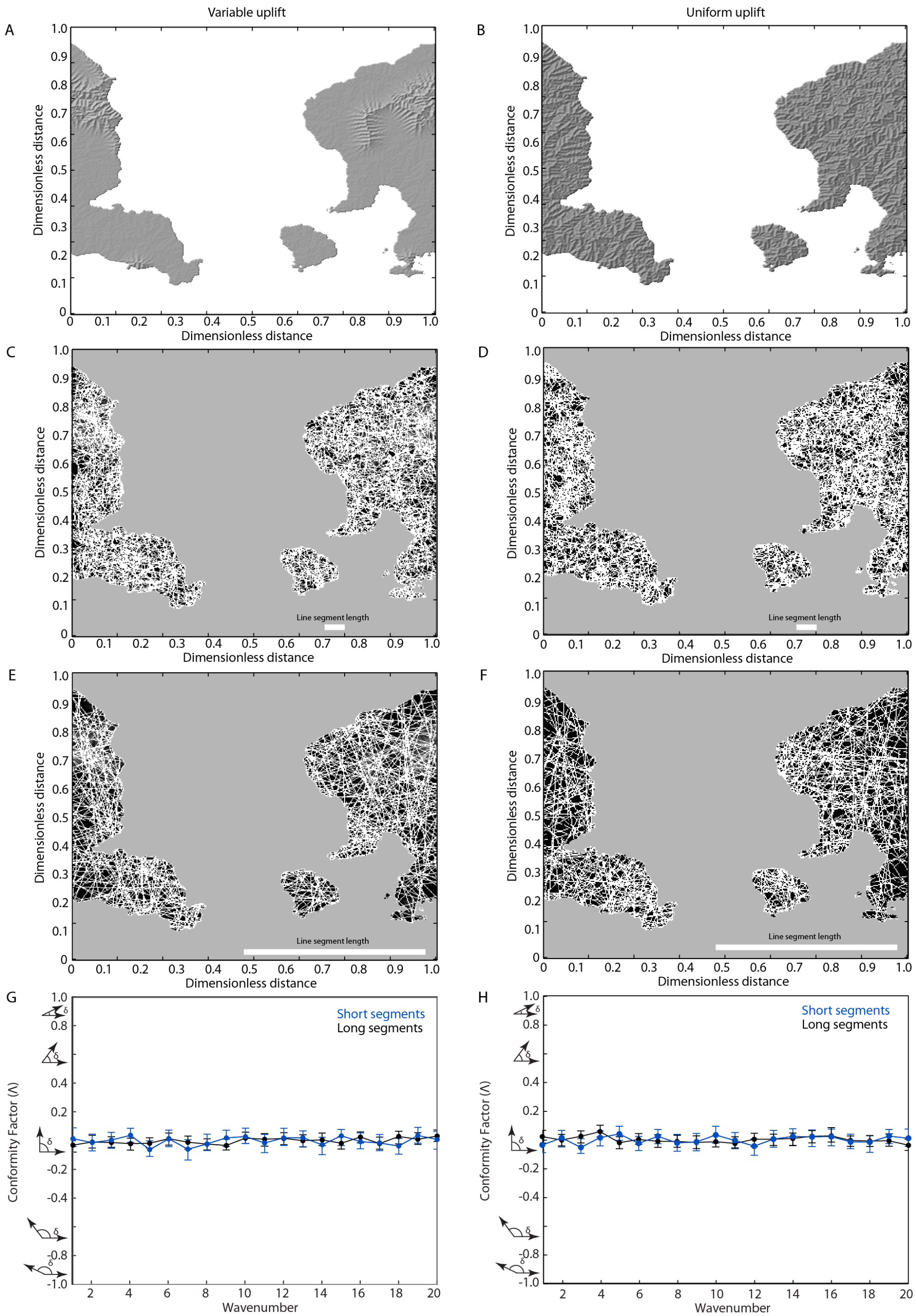

Fig. S2. Synthetic tests to identify any bias related to the scale of measured drainages. (A) Shaded relief map of model topography produced with spatially variable uplift. **(B)** As in A, but for spatially uniform uplift. **(C)** Short synthetic drainages, superposed on outline of topography from A. **(D)** As in C, but with spatially uniform uplift from B. **(E)** As in C, but with long synthetic drainages **(F)** As in E, but for uniform uplift. **(G)** Topographic conformity Λ for synthetic dataset with spatially variable uplift. **(H)** Topographic conformity Λ for synthetic dataset with spatially uniform uplift. Error bars correspond to the 95% confidence interval for the median.

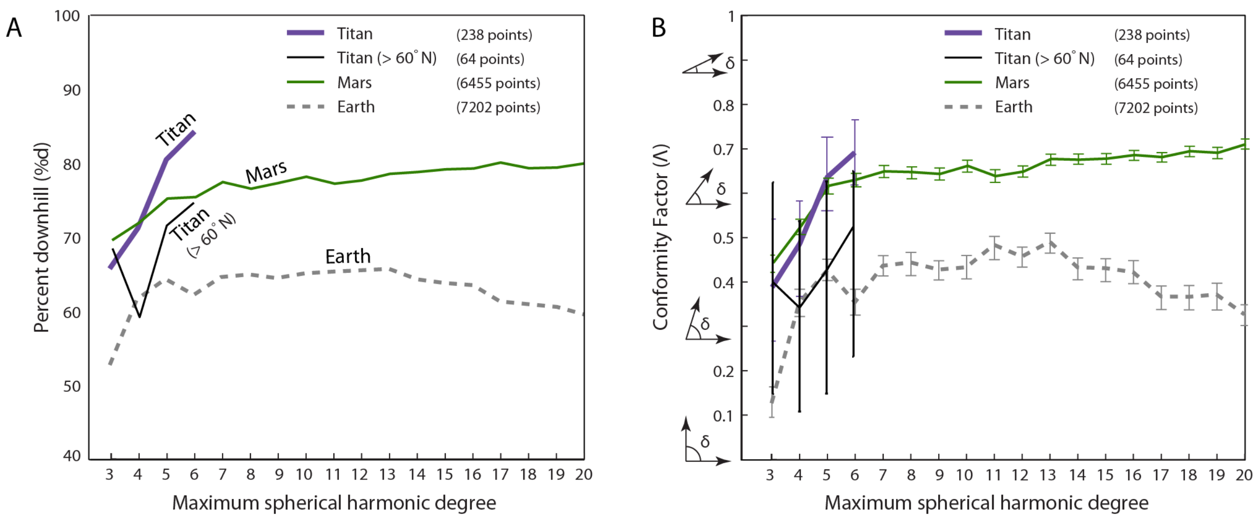

Fig. S3. Long-wavelength topographic conformity is lower in Titan's north polar region. As in Fig. 2, but including Titan's north polar region (defined here as the region northwards of 60°N). Error bars in (B) correspond to the 95% confidence interval for the median. The median conformity factor values for Titan's north polar region at degrees 4-6 are lower than those for Titan as a whole. Given the small sample size, the 95% confidence intervals overlap, but the offset in median values supports differences in the geologic history of Titan's north polar region relative to the rest of Titan.

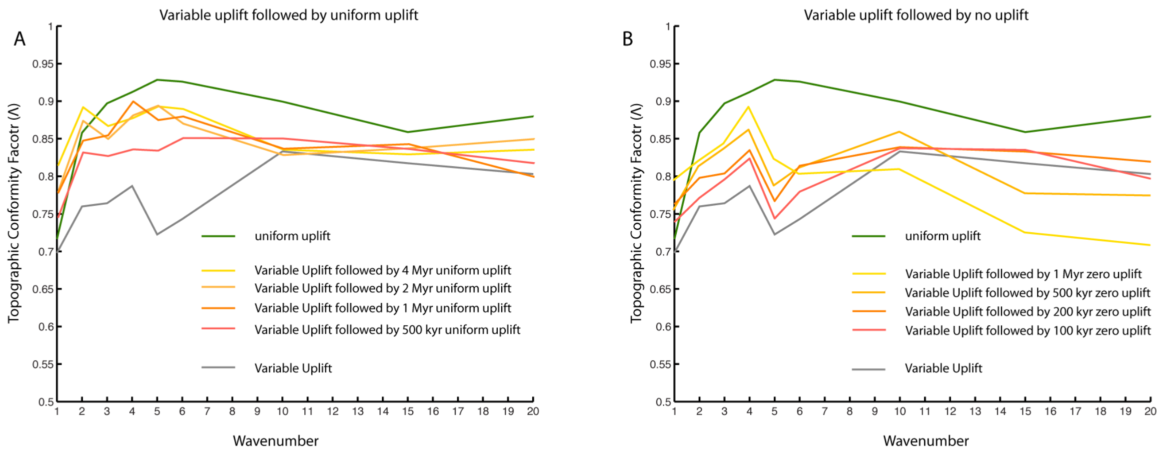

Fig. S4. Drainage networks and deformation interact through time. To investigate how temporal variations in the pattern of deformation influence topographic conformity, we conducted simulations in which variable uplift (which represents dominantly short-wavelength deformation associated with plate tectonics) gave way to either **(A)** uniform uplift, which represents dominantly long-wavelength deformation, or **(B)** zero uplift, which represents tectonic quiescence. Curves represent individual simulations. We find that low Λ is a signature of actively generated variable-uplift plate tectonics. If variable uplift is followed by uniform uplift, then the signature of that variable uplift will gradually be erased. If variable uplift is followed by zero uplift, then Λ increases at first as drainages conform with topography. Ultimately, landscapes where virtually all relief has been erased can also display poor topographic conformity.

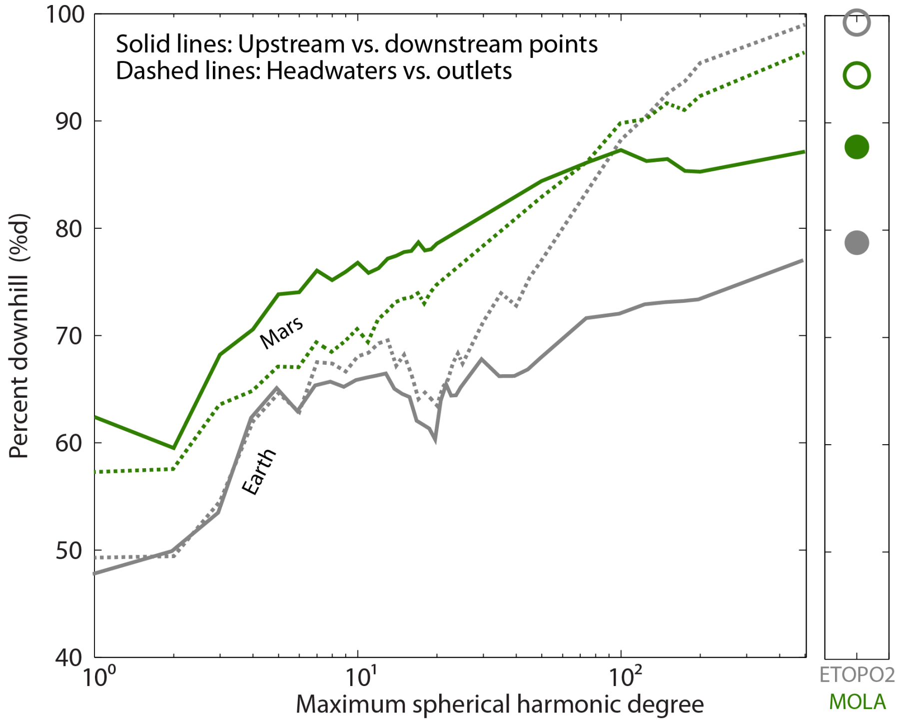

Fig. S5. Differences in topographic conformity on Mars versus Earth extend to shorter wavelengths. Solid lines (and filled circles in right panel) show the percent of points that are uphill (according to the topography at a given spherical harmonic degree) of the nearest downstream point. Dashed lines (and empty circles in right panel) show the percent of headwaters that are uphill (according to the topography at a given spherical harmonic degree) of the drainage network outlet. Small panel at right shows the same metrics computed for the ETOPO2 gridded 2-minute global relief dataset for Earth *(55)* and four pixel-per-degree MOLA topography for Mars *(37)*. We expect *%d* to reach 100% when topography is perfectly resolved, drainage networks are perfectly delineated, and drainages have not experienced deformation after the era of fluvial activity. On Earth, the delineation of fluvial features was performed at 1/8 degree resolution from HydroSHEDS and Hydro1k data *(17)*, distinct from the higher resolution ETOPO2 dataset, resulting in slight misalignments at the scale at which fluvial valleys are resolved. These misalignments do not affect long wavelength topographic conformity, because fluvial valleys are not resolved at these wavelengths. We attribute the plateau in %d on Mars to deformation after incision of valley networks *(24, 25)*. For Earth and Mars, calculation of *%d* for the headwaters versus outlet of each drainage shows that *%d* values on Earth converge to 100% across the scale of the drainage, whereas *%d* values on Mars reach ~95%.

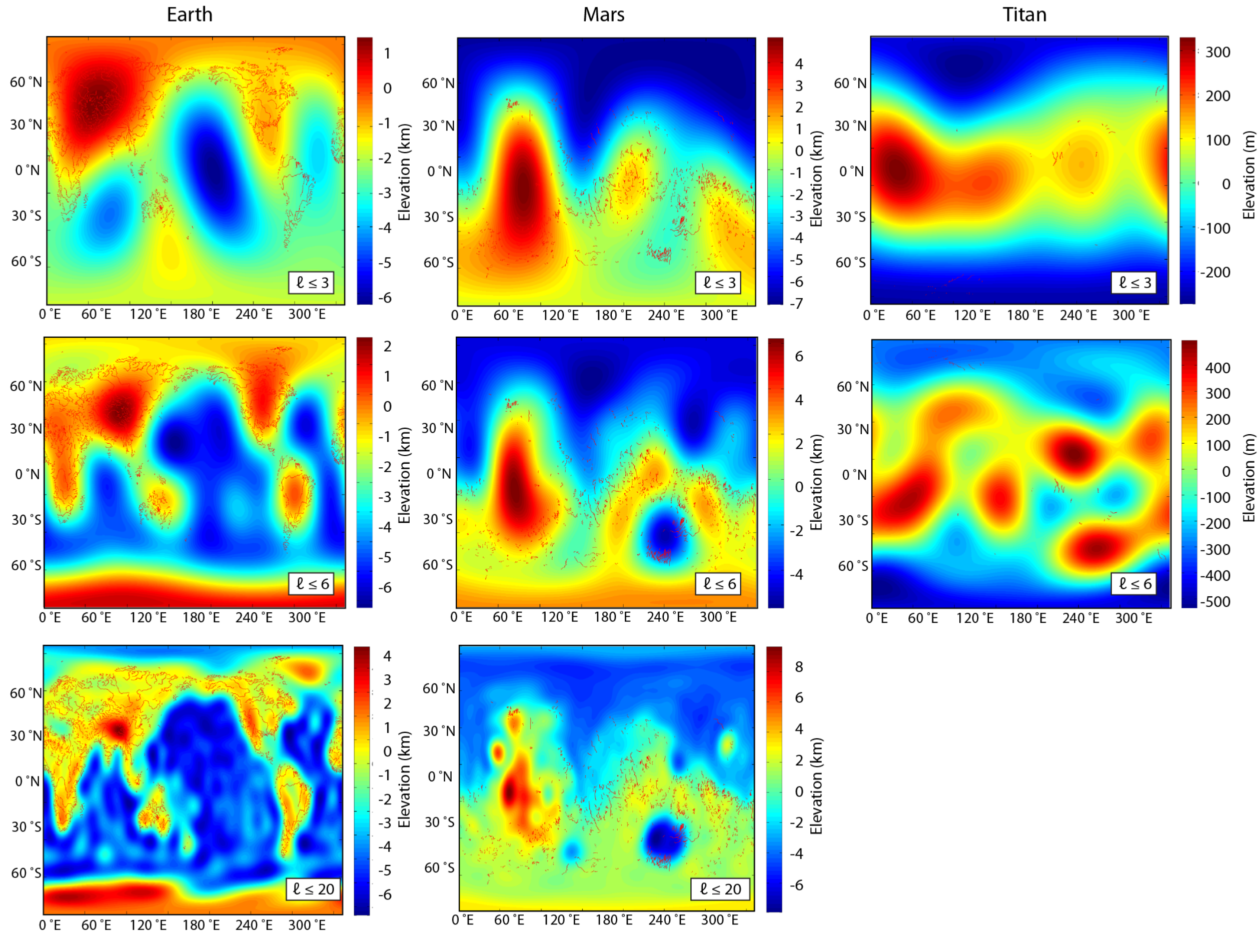

Fig. S6. Spherical harmonic models for the topography of Titan, Earth, and Mars. For Earth and Mars, we show maximum spherical harmonic degrees (ℓ) of 3,6, and 20. At present, topography is not well constrained for ℓ>6 for Titan *(21)*. Coloring reflects elevation referenced to the geoid.

611

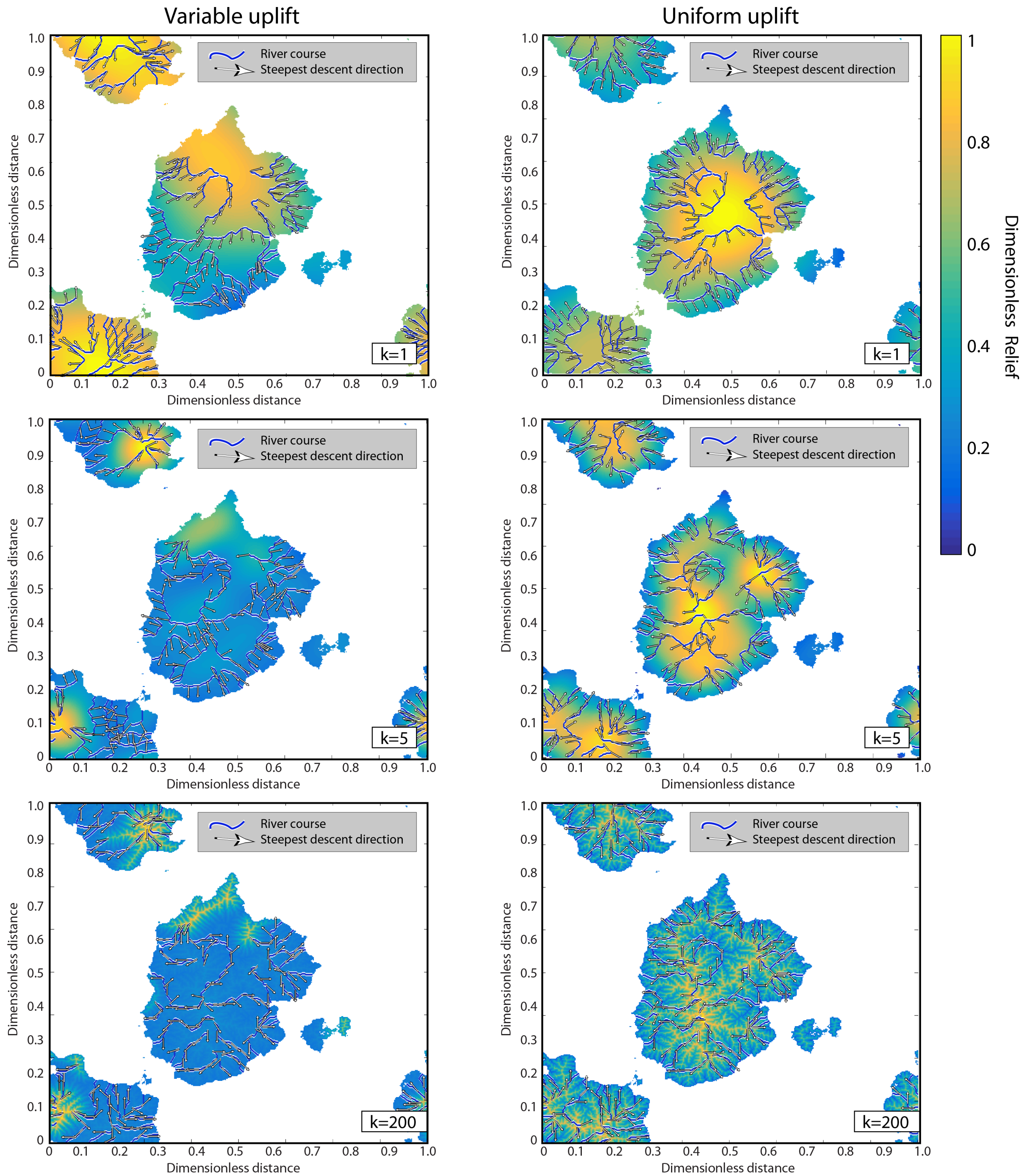

Fig. S7. Example model topography, filtered to increasing maximum spectral wavenumbers. We show the model state at the conclusion of variable uplift (left column) and uniform uplift (right column) runs with identical initial conditions. We filter the topography to maximum spectral wavenumbers of *k*=1, *k*=5, and *k*=200 wavelengths across the domain, as indicated on each panel.

612

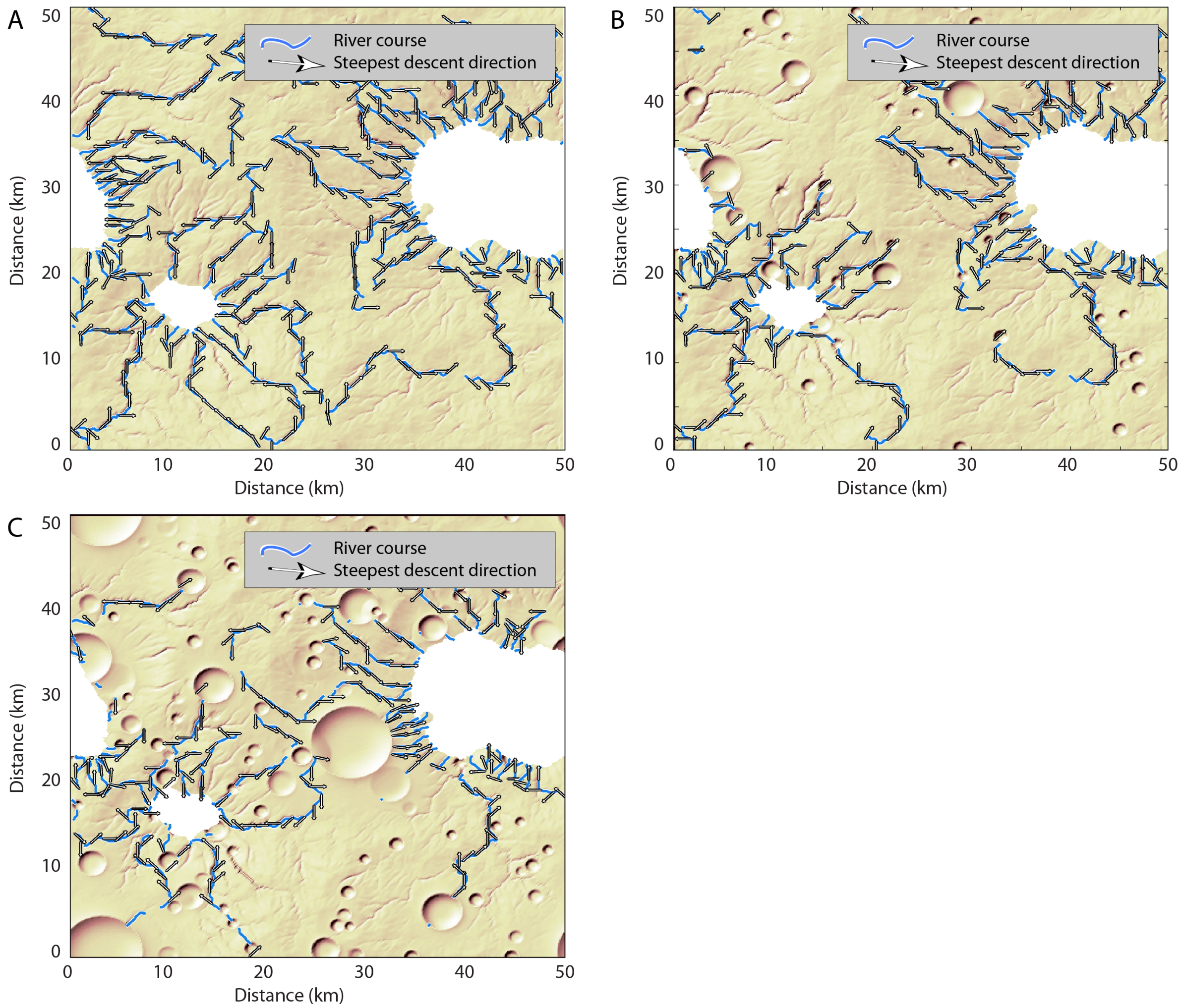

Fig. S8. Shaded relief maps of landscape evolution simulations with cratering. We ran three ensembles (each with ten simulations spanning 60 Myr) to examine the influence of impact cratering on topographic conformity. **(A)** In the control ensemble, fluvial erosion of an initially uncratered surface proceeded without interference. **(B)** We considered fluvial erosion of the same initial surfaces in the control ensemble, but with impact topography superposed on the initial surface as described in the Materials and Methods. **(C)** We also considered fluvial erosion of the same cratered initial surfaces, but with further impacts that occurred during the course of our simulations, disrupting the topography (note the presence of truncated valley networks). This simulation is also shown in Fig. 4A. Each snapshot shows the state of the simulation after 60 Myr.

Table S1. Landscape evolution modeling parameters.

Parameter	Value	Notes
Lateral grid dimensions	400 × 400	
Enhanced uplift relative to background uplift	10	Only in variable uplift simulations
Steam power coefficient *K*	5×10^{-6} $m^{(1-2m)}$ yr^{-1}	
Drainage area exponent *m*	0.5	ref. *(40)*
Slope exponent *n*	1.0	ref. *(41)*
Critical slope	0.6	
Slope of the power spectrum of initial red noise topography	2.0	ref. *(27)*
Fraction of initial topography assigned to be a fixed base level (to represent oceans)	0.7	
Slope of the power spectrum of red noise surface used to define zones of enhanced uplift in variable uplift simulations	1.3	Only in variable uplift simulations. Less positive values translate to more variance at shorter wavelengths
Fraction of this surface assigned to experience enhanced uplift in variable uplift simulations	0.35	Only in variable uplift simulations.
Simulation duration	10 Myr	

Table S2. Landscape evolution modeling parameters for impact cratering simulations.

Parameter	Value	Notes
Lateral grid dimensions	400 × 400	
Lateral grid spacing	125 m × 125 m	
Steam power coefficient *K*	1×10^{-8} $m^{(1-2m)}$ yr^{-1}	
Drainage area exponent *m*	0.5	ref. *(40)*
Slope exponent *n*	1.0	ref. *(41)*
Critical slope	0.6	
Slope of the power spectrum of initial red noise topography	2.0	ref. *(27)*
Fraction of initial topography assigned to be a fixed base level (to represent lakes or oceans)	0.1	
Simulation duration	60 Myr	

Database S1. Source and sink coordinates for analyzed drainage networks on Titan (see Excel file with tabulated coordinates).